Numerical analysis of ballistic-electron transport in magnetic fields by using a quantum point contact and a quantum wire

T. Usuki,* M. Saito, M. Takatsu, R. A. Kiehl, and N. Yokoyama
Quantum Electron Devices Laboratory, Fujitsu Laboratories Ltd., 10-1 Morinosato-Wakamiya, Atsugi 243-01, Japan
(Received 10 January 1995)

We report the numerical analysis of our experimental results for electron-wave propagation from a quantum point contact to a quantum wire. Our numerical method solves the boundary problem of a lattice model, and determines wave functions at an arbitrary site. This method also includes a recursive Green's-function method. Our study found oscillations in the conductance, and magnetic suppression of those oscillations. For a simple model, we simulate the oscillations directly related to the channel number in the quantum wire. To understand the magnetic suppression, we investigate the dependence of the electron-wave propagation on the magnetic field using a realistic model. Numerical results show that a realistic rounded corner at the point-contact and a magnetic field could suppress the oscillations. We also discuss the transition from a classical skipping orbit with clear circular segments and focusing to a quantum edge state along a potential wall.

I. INTRODUCTION

Mesoscopic systems have interesting electrical transport characteristics due to their coherent ballistic electrons. For example, we can give the following: conductance quantization (in a point contact),[1,2] magnetic focusing,[3] and Hall effect for a one-dimensional (1D) crosswire.[4,5] These mesoscopic phenomena have been measured in an artificial system with a variable confining potential. Many systems have been fabricated using submicron lithography and high-mobility two-dimensional (2D) electron gas structures. In these systems, the dimensions are significantly smaller than both the mean-free path and the coherent length at low temperatures. There have also been many theoretical studies of the mesoscopic phenomena of electron-wave interference and ballistic trajectories. Conductance quantization has already been explained clearly,[6,7] and numerical calculations have shown the ideal skipping orbit for magnetic focusing.[8,9] Numerical analysis has pointed out that the shape of the device strongly affects its transport characteristics. For example, the Hall effect in a 1D crosswire is defined by the shape of the crossing.[10,11] Other examples have predicted the chaotic resistance fluctuations due to scattering from a geometric feature.[12,13]

In this paper, we present a numerical analysis of our experimental data for the mesoscopic system. We detail the dependence of the transport characteristics on the subject's shape. We measured the transport characteristics of a device with a point contact and a reflector.[14] Figure 1(a) shows our device and circuit when we measured the point-contact resistance. The device was fabricated on a modulation-doped $Al_xGa_{1-x}As/GaAs$ heterostructure epilayer. The mean-free-path length was 4.5 μm and the Fermi wavelength was 44 nm at 0.34 K. This device's dimensions are less than the mean-free-path length; the electrons are expected to move in this device nearly bal-

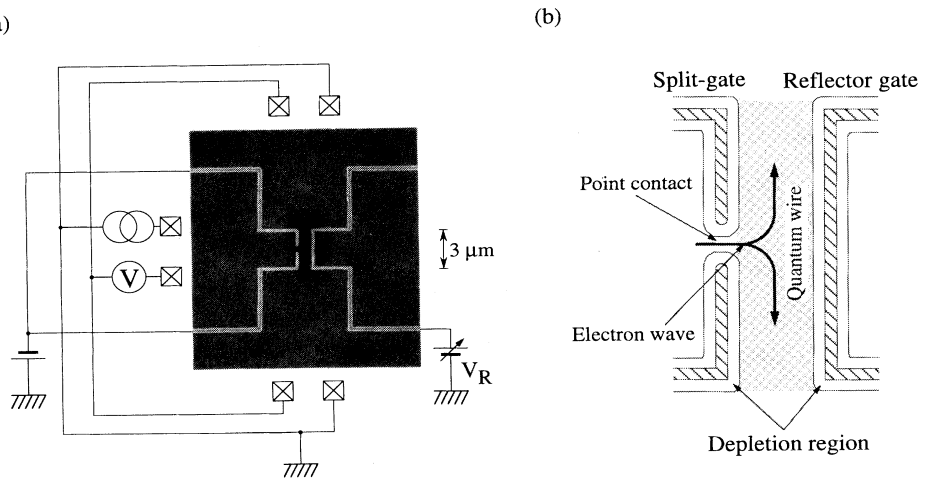

FIG. 1. (a) A scanning electron microscope micrograph of our device with control and measurement circuits for point-contact resistance. (b) Diagram of a confinement structure with a point contact and a reflector. The shaded region indicates a quantum wire with 1D channels, where the 1D channel number is controlled by changing the voltage V_R.

0163-1829/95/52(11)/8244(12)/$06.00

listically. The measurement temperature and applied current were low; therefore, the phase coherence length is expected to be comparable to the device's dimensions.[15] Figure 1(b) shows both gate structures and the depletion regions. The electron gas system confined by these depletion regions has a T-shaped configuration that consists of a point contact and a quantum wire along the reflector. The point-contact opening was fixed, as it has a maximum of two channels. That is, we fixed the voltage applied to the split gate. The shaded region in Fig. 1(b) is the quantum wire, and its width was controlled by changing the voltage V_R applied to the reflector gate. Accordingly, our devices have only two geometrical parameters; the width of the point contact, and the separation between the point contact and the reflector. These parameters could be evident from measuring the conductance quantization. This advantage allows us to carry out a more detailed analysis of the experimental results than in other device structures.[16,17] We measured the point-contact resistance with changing V_R by using the circuit in Fig. 1(a). For monitoring the channel number in the wire, we also measured the four-terminal quantum wire conductance, where we floated two terminals at the left side in Fig. 1(a). The point-contact resistance in Fig. 2(a) is periodic where there is no magnetic field, and the periodicity relates to the channel number in the wire, as evident from the quantum wire conductance in Fig. 2(b). The magnetic field completely suppressed the oscillation at 0.2 T. The oscillation was suppressed, but the conductance quantization of the wire remained, even in a magnetic field.[14]

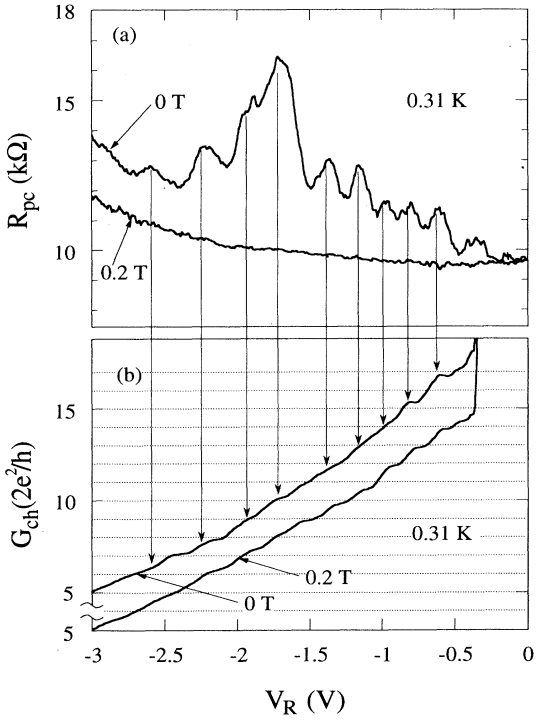

FIG. 2. Experimental results at 0.31 K with changing V_R. (a) Point-contact resistance with oscillations. (b) Conductance of the quantum wire, where we floated two terminals at the left side in Fig. 1(a). The conductance quantization means monitoring the 1D channel number in the wire. The oscillations are completely suppressed by a magnetic field. Nevertheless, the conductance quantization remains while in the magnetic field.

To analyze these properties, we numerically investigated electron-wave transport of a T-shaped structure in a magnetic field. A detailed analysis required a calculation method that could obtain both conductance and spatial information of a 2D electron system with complex potential profile. Our numerical analysis used a method for solving the boundary problem of a lattice model, and for obtaining wave functions at an arbitrary site. A method has already been developed to study mesoscopic phenomena for a line-shaped, point-contact injector and a wedge-shaped, point-contact detector.[18] We apply this method to the lattice model in our paper. This method includes the recursion using the Green's function.[19–21] Details of the calculation method are given in Sec. II. In Sec. III, we apply this method to our geometry with an ideal abrupt configuration, and we discuss the clear conductance oscillation. Section IV gives numerical results for a realistic structure, and the numerical results show the magnetic suppression of the oscillations. Numerical calculations also show an interesting magnetic property, a transition from a classical skipping orbit to a quantum edge state with changing magnetic fields. A summary is given in Sec. V.

II. CONDUCTANCE CALCULATION IN 2D LATTICE MODEL

We can investigate the transport phenomena in mesoscopic systems by using the Landauer-Büttiker formula.[22,23] To obtain the conductance, we have studied a numerical method for calculating stably transmission coefficients.[18] We now explain how the method expands to a 2D square lattice model by considering a quantum wire.

The quantum-wire lattice model consists of a scattering

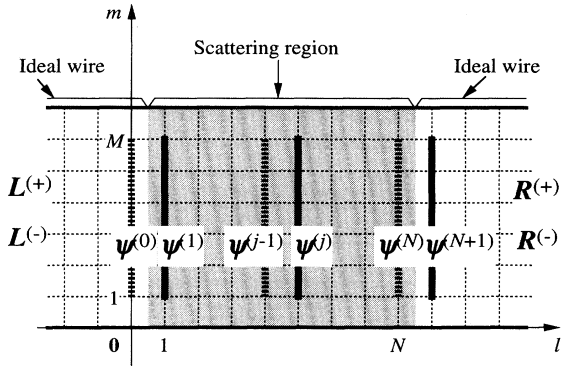

FIG. 3. Configuration of a lattice model for a quantum wire. Integer coordinates (l,m) mean lattice points, and the lattice constant is taken as a unit of length. This model consists of a scattering region and two ideal wires of width $M+1$.

region and two ideal wires with a width of $M+1$, as shown in Fig. 3. The coordinates (l,m) are the lattice points. The lattice constant is taken as being a unit of length. The Hamiltonian of this model is given by

$$H=\sum_l \mathbf{a}_l^+(\mathbf{H}_l-E_F)\mathbf{a}_l+\mathbf{a}_l^+\mathbf{H}_{l,l+1}\mathbf{a}_{l+1} +\mathbf{a}_l^+\mathbf{H}_{l,l-1}\mathbf{a}_{l-1} , \tag{2.1}$$

where $\mathbf{a}_l$ is the column vector of annihilation operators a_{lm} for a site state $\mathbf{a}_l={}^T(a_{l1},\ldots,a_{lM})$. Here, $\mathbf{H}_l$, $\mathbf{H}_{l,l-1}$, and $\mathbf{H}_{l,l+1}$ are $M\times M$ matrices defined by

$$\mathbf{H}_l=\begin{bmatrix} V_{l1}+4t & -t & 0 & \cdots & 0 \\ -t & V_{l2}+4t & -t & \cdots & 0 \\ 0 & -t & V_{l3}+4t & \cdots & 0 \\ \vdots & \vdots & \vdots & \ddots & \vdots \\ 0 & 0 & 0 & \cdots & V_{lM}+4t \end{bmatrix} , \tag{2.2}$$

$$\mathbf{H}_{l,l-1}=\mathrm{diag}[-t\exp(2\pi i\tilde{B}),\ldots,-t\exp(2\pi i\tilde{B}M)] , \tag{2.3}$$

and

$$\mathbf{H}_{l,l+1}=\mathbf{H}_{l,l-1}^* . \tag{2.4}$$

In Eqs. (2.2) and (2.3), the nearest-neighboring integral and site energy are given by $-t$ and V_{lm}, respectively. The magnetic field $\tilde{B}$ is included in terms of a Peirls phase factor. $\tilde{B}$ can be specified by a Fermi wavelength λ_F and a cyclotron radius R_c:

$$\tilde{B}=1/\lambda_F R_c . \tag{2.5}$$

In the following numerical calculation, we set λ_F to 10, since this is long enough for a lattice constant. The Fermi energy E_F and λ_F follow

$$E_F=2t\left[1-\cos\left[\frac{2\pi}{\lambda_F}\right]\right] . \tag{2.6}$$

The wave function Ψ in the system is defined by the above Hamiltonian as $H|\Psi\rangle=0$. In particular, $2M$ channels are formed in the ideal wires since the site potential V_{lm} in the region of the ideal wires is not dependent on position l. Then, to study the scattering problem of the wave function, we consider the channel coefficient $\mathbf{L}(\pm)$ in the ideal wire on the left and $\mathbf{R}(\pm)$ in the ideal wire on the right, where $+$ $(-)$ refer to waves moving to the right (left). These coefficients are represented by a column vector with M elements, and satisfy the following equation:

$$\begin{bmatrix}\mathbf{R}(+)\\ \mathbf{R}(-)\end{bmatrix}=\mathbf{T}_0^{-1}\mathbf{T}_N\cdots\mathbf{T}_0\begin{bmatrix}\mathbf{L}(+)\\ \mathbf{L}(-)\end{bmatrix} . \tag{2.7}$$

We define $\boldsymbol{\psi}^{(l)}$ as a column vector describing the wave function of the lth cell consisting of M sites. The $(2M\times 2M)$ matrix $\mathbf{T}_l$ satisfies the following:

$$\begin{bmatrix}\boldsymbol{\psi}^{(0)}\\ \boldsymbol{\psi}^{(1)}\end{bmatrix}=\mathbf{T}_0\begin{bmatrix}\mathbf{L}(+)\\ \mathbf{L}(-)\end{bmatrix} , \tag{2.8}$$

$$\begin{bmatrix}\boldsymbol{\psi}^{(l)}\\ \boldsymbol{\psi}^{(l+1)}\end{bmatrix}=\mathbf{T}_l\begin{bmatrix}\boldsymbol{\psi}^{(l-1)}\\ \boldsymbol{\psi}^{(l)}\end{bmatrix} \quad \text{for} \quad 1\le l\le N , \tag{2.9}$$

and

$$\begin{bmatrix}\mathbf{R}(+)\\ \mathbf{R}(-)\end{bmatrix}=\mathbf{T}_0^{-1}\begin{bmatrix}\boldsymbol{\psi}^{(N)}\\ \boldsymbol{\psi}^{(N+1)}\end{bmatrix} . \tag{2.10}$$

The matrix $\mathbf{T}_0$ is given by

$$\mathbf{T}_0=\begin{bmatrix}\mathbf{U}(+) & \mathbf{U}(-)\\ \mathbf{U}(+)\boldsymbol{\lambda}(+) & \mathbf{U}(-)\boldsymbol{\lambda}(-)\end{bmatrix} , \tag{2.11}$$

with

$$\mathbf{U}(\pm)=[\mathbf{u}_1(\pm),\ldots,\mathbf{u}_M(\pm)] , \tag{2.12}$$

and

$$\boldsymbol{\lambda}(\pm)=\mathrm{diag}(\lambda_1(\pm),\ldots,\lambda_M(\pm)) . \tag{2.13}$$

$\mathbf{u}_m$ is a column vector describing the amplitude of the mth channel for M sites along the m axis, and λ_m is a phase factor of a plane wave along the l axis for the mth channel. The column vector and the phase factor are given by solving the eigenvalue equation below:

$$\begin{bmatrix}\mathbf{0} & \mathbf{1}\\ -\mathbf{H}_{0,1}^{-1}\mathbf{H}_{0,-1} & \mathbf{H}_{0,1}^{-1}(E_F-\mathbf{H}_0)\end{bmatrix}\begin{bmatrix}\mathbf{u}_m(\pm)\\ \lambda_m(\pm)\mathbf{u}_m(\pm)\end{bmatrix} =\lambda_m(\pm)\begin{bmatrix}\mathbf{u}_m(\pm)\\ \lambda_m(\pm)\mathbf{u}_m(\pm)\end{bmatrix} . \tag{2.14}$$

In the following discussion, the column vector $\mathbf{u}_m$ is normalized as $\|\mathbf{u}_m\|=1$. The matrix $\mathbf{T}_l$ for $1\le l\le N$ is given by

$$\mathbf{T}_l=\begin{bmatrix}\mathbf{0} & \mathbf{1}\\ -\mathbf{H}_{l,l+1}^{-1}\mathbf{H}_{l,l-1} & \mathbf{H}_{l,l+1}^{-1}(E_F-\mathbf{H}_l)\end{bmatrix} . \tag{2.15}$$

The whole wave function from one outer region to another is simply solved by using Eqs. (2.8)–(2.10). We can also obtain the transmission probability $|t_{nm}|^2$ from the incident channel m with velocity v_m to the outgoing channel n with velocity v_n. In terms of the transmission probability, the conductance G of the system is obtained from a multichannel version of the Landauer-Büttiker formula[24] below

$$G=\frac{2e^2}{h}\sum_{m,n}\frac{v_n}{v_m}|t_{nm}|^2 . \tag{2.16}$$

The matrix $\mathbf{t}$ of the transmission wave is defined by

$$\begin{bmatrix}\mathbf{t}\\ \mathbf{0}\end{bmatrix}=\mathbf{T}_0^{-1}\mathbf{T}_N\cdots\mathbf{T}_0\begin{bmatrix}\mathbf{1}\\ \mathbf{r}\end{bmatrix} . \tag{2.17}$$

Note that the above equation is extremely unstable in general. We stabilize it by using the following iteration technique:

$$\begin{bmatrix} \mathbf{C}_1^{(l+1)} & \mathbf{C}_2^{(l+1)} \\ \mathbf{0} & \mathbf{1} \end{bmatrix} = \mathbf{T}_l \begin{bmatrix} \mathbf{C}_1^{(l)} & \mathbf{C}_2^{(l)} \\ \mathbf{0} & \mathbf{1} \end{bmatrix} \mathbf{P}_l \quad \text{for } 0 \le l \le N+1 , \tag{2.18}$$

with

$$\mathbf{T}_{N+1} = \begin{bmatrix} \mathbf{0} & [\mathbf{U}(+)\boldsymbol{\lambda}(+)]^{-1} \\ \mathbf{1} & -\mathbf{U}(+)[\mathbf{U}(+)\boldsymbol{\lambda}(+)]^{-1} \end{bmatrix} \tag{2.19}$$

and

$$\mathbf{P}_l = \begin{bmatrix} \mathbf{1} & \mathbf{0} \\ \mathbf{P}_{l1} & \mathbf{P}_{l2} \end{bmatrix} . \tag{2.20}$$

An initial condition of the iteration is $\mathbf{C}_1^{(0)}=\mathbf{1}$, $\mathbf{C}_2^{(0)}=\mathbf{0}$, and $\mathbf{T}_{N+1}$ is added to $\mathbf{T}_l$. Matrix $\mathbf{P}_l$ is a linear operator to satisfy the form that is assigned to the matrix on the left of Eq. (2.18). Then we treat this linear operator for each connecting step in the computation. The detailed expressions are given by

$$\mathbf{P}_{l1} = -\mathbf{P}_{l2}\mathbf{T}_{l21}\mathbf{C}_1^{(l)} \tag{2.21}$$

and

$$\mathbf{P}_{l2} = [\mathbf{T}_{l21}\mathbf{C}_2^{(l)} + \mathbf{T}_{l22}]^{-1} , \tag{2.22}$$

where

$$\mathbf{T}_l = \begin{bmatrix} \mathbf{T}_{l11} & \mathbf{T}_{l12} \\ \mathbf{T}_{l21} & \mathbf{T}_{l22} \end{bmatrix} . \tag{2.23}$$

This iteration continues from $l=0$ to $N+1$, and it finally gives $\mathbf{t}=\mathbf{C}_l^{(N+2)}$. A similar iteration gives the matrix $\mathbf{r}$ of the reflection wave as

$$(\mathbf{D}_1^{(l+1)}\mathbf{D}_2^{(l+1)}) = (\mathbf{D}_1^{(l)}\mathbf{D}_2^{(l)})\mathbf{P}_l \quad \text{and} \quad \mathbf{r}=\mathbf{D}_1^{(N+2)} , \tag{2.24}$$

where the initial condition is $\mathbf{D}_1^{(0)}=\mathbf{0}$, $\mathbf{D}_2^{(0)}=\mathbf{1}$. In order to obtain the electron density at a point, we define a row vector and calculate as follows:

$$(\psi_1^{(l)}(l,m), \ldots, \psi_{2M}^{(l)}(l,m)) \equiv (0, \ldots, 0, \delta_{m1}, \ldots, \delta_{mM}) \tag{2.25}$$

and

$$(\psi_1^{(j+1)}(l,m), \ldots, \psi_{2M}^{(j+1)}(l,m)) = (\psi_1^{(j)}(l,m), \ldots, \psi_{2M}^{(j)}(l,m))\mathbf{P}_j \quad \text{for} \quad l \le j \le N+1 . \tag{2.26}$$

Then the position probability density is obtained by

$$n_i(l,m) = |\psi_i^{(N+2)}(l,m)|^2 , \tag{2.27}$$

where the parameter i refers to the left channel number, the injected channel.

The iterative technique is useful for obtaining stable calculations, because it cancels divergence factors that occur due to the rounding errors of each step. When the method is slightly modified, it becomes as applicable as the well-known Green's-function method[19–21] (see Appendix). The advantage over the Green's-function method is that the transmission matrix, reflection matrix, and wave function at any point can be obtained simultaneously by the linear operator $\mathbf{P}_l$. Calculating the position probability density is important in understanding both electron wave propagation and mesoscopic device design. The numerical calculation of $\mathbf{P}_l$ spends the same size as obtaining the Green's function in our case.

We would normally investigate the electron-wave propagation in our experimental results using this feature. However, the lattice model of the simple quantum-wire structure has to be extended to a structure suitable for our device. As shown in Fig. 4, we use a T-shaped structure consisting of a wire A of width $L+1$ and a wire B of width $M+1$, so that the lattice size is defined by two parameters, L and M. Wire A and wire B are related to our device's point contact and quantum wire along the reflector in Fig. 1(b), respectively. The T-shaped structure is a kind of three-terminal device. To analyze the transport of this structure, we should use the three-terminal Landauer-Bütiker formula in general.[23] However, for the point-contact conductance by our circuit in Fig. 1(a), the three-terminal formula can be reduced to the two-terminal formula, because the chemical potential of a terminal in wire B is equal to that of another terminal in wire B (see Fig. 4). Then we use Eq. (2.16) where the outgoing channels are defined by channels toward two terminals in wire B. The iteration method can also be applicable to the T-shaped structure by extending all matrices and changing suitable gauge when $l=1$. In the following section, we show numerical results from our method.

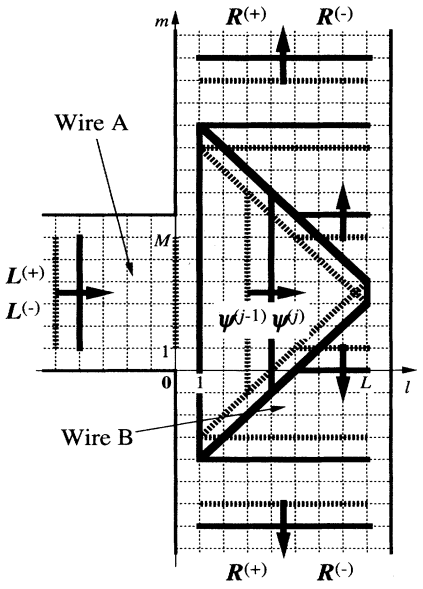

FIG. 4. Configuration of a T-shaped structure lattice model for our experimental device. This structure consists of a wire A with width $M+1$ and a wire B with width $L+1$. Wire A is the point contact in Fig. 1 and wire B is the quantum wire in Fig. 1.

III. T-SHAPED STRUCTURE WITH ABRUPT CONFIGURATION

We measured the oscillations of conductance for a point contact with a reflector as shown in Fig. 1.[14] To understand a property of the oscillation, we initially try calculating the conductance of a T-shaped structure with a hard-well potential and an abrupt configuration initially. It seems that the complex multiscattering of electron waves rarely occurs in this structure, compared to a realistic structure. Therefore, we can easily derive a simple picture of the oscillation in the simple T-shaped structure.

As shown in Fig. 4, the T-shaped structure has two basic parameters, L and M. Wire A of width $M+1$ is regarded as the injector of a point contact in Fig. 1. Parameter M is set $M=20$ with $\lambda_F=10$.[25] Wire B of width $L+1$ is the quantum wire made by the split gate and the reflector gate in Fig. 1. Changing parameter L refers to changing the applied voltage of our reflector. Figure 5 shows the relationship between the conductance, from the injector to the infinite wire, with changing L. When an electron wave is injected through the first channel in wire A, in Fig. 5(a), the conductance oscillation corresponds well with a period of forming channels below the Fermi level in wire B, as shown in Fig. 5(c). The angular distribution of the injected wave through the second channel is wider than through the first channel,[8,18,25] because the kinetic energy for the confining (flowing) direction in the second channel is higher (lower) than the first channel. Accordingly, by injecting the wave through the

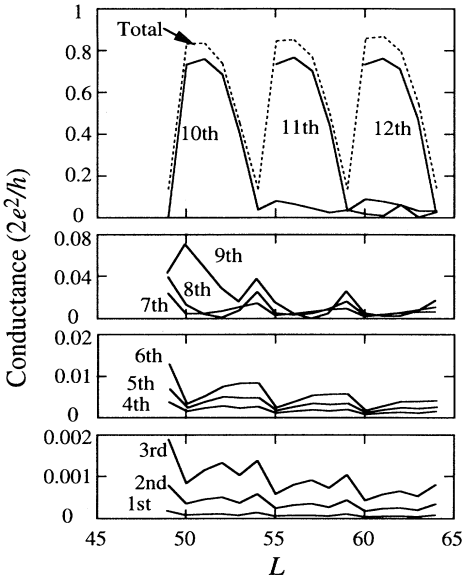

FIG. 6. Conductance contributing to each channel in wire B, where the broken line shows the total conductance. The periodic oscillation is mainly defined by matching the injected wave function against a channel just below the Fermi level.

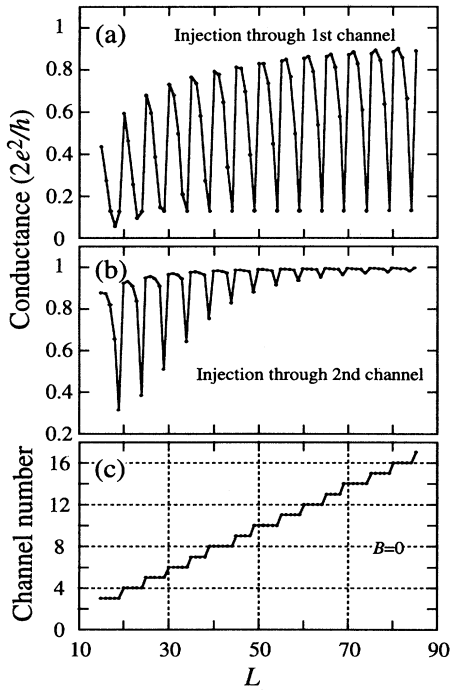

FIG. 5. Conductance from wire A with $M=20$ to wire B by changing L, for an ideal abrupt structure. We set a Fermi wavelength $\lambda_F=10$. (a) Injecting electron waves through the first channel and (b) through the second channel. (c) The channel number in wire B. The conductance clearly shows an oscillation for a period of forming channels below the Fermi level in wire B.

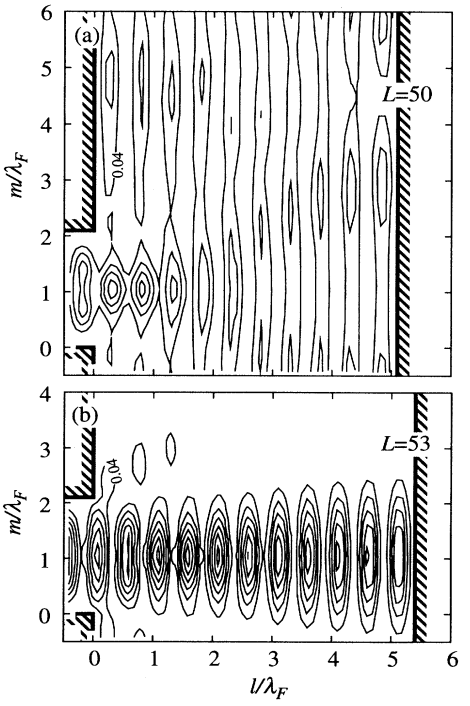

FIG. 7. Position probability density for the ideal abrupt structure. (a) $L=50$; matching case. (b) $L=53$; not matching case.

second channel in wire A, the conductance, of which the oscillation becomes smaller, is higher than through the first channel [see Figs. 5(a) and 5(b)]. We think that the oscillation is caused by a matching between the channels in the infinite wire and a wave function consisting of injecting and reflecting waves. Figure 6 shows the conductance contributing to each channel in wire B, related to Fig. 5(a). As is evident from Fig. 6, the total conductance and the oscillations are mainly defined by matching the injected-wave function with a channel just below the Fermi level.[14] The conductance oscillates for a period of half a Fermi wavelength. The distribution of electron waves in real space helps in understanding the ballistic transport of a mesoscopic system. Figure 7 shows the position probability density $L=50$ (matching case) and $L=53$ (not matching case). This figure shows that maximum conductance occurs at matching channels in wire B, and the mode formed by injecting and reflecting waves.

We calculate the conductance in a magnetic field with $R_c/\lambda_F=10$. This corresponds to 0.2 T in our experiment. In Fig. 8(a), the oscillations become slightly smaller than in no magnetic field. When an electron wave is injected through the second channel in wire A, the oscillations become larger than in no magnetic field in Fig. 8(b). Obviously, these results are different from the magnetic suppression in our experiment [Fig. 2(a)].

We obtain a simple picture of the oscillation in the matching electron waves. However, the simple T-shaped structure with an abrupt configuration cannot explain all the properties of our experimental results.

IV. PROPAGATION IN REALISTIC STRUCTURE

Previous numerical studies obtained the propagation of electron waves for only a simple abrupt structure, composed of wires with hard walls.[14] The propagation in realistic structures has not been investigated thoroughly, although we know it is sensitive to the shape. The following numerical results clearly show that the interpretation of an actual experimental ballistic transport needs calculation that account for complex multiscattering. We examined a T-shaped structure with a realistic potential profile.

A. Conductance oscillations with rounded shape

It has been reported that the confinement potential of the quantum wire caused by a split gate has a parabolic shape.[26] Based on our previous report,[18] we assume that

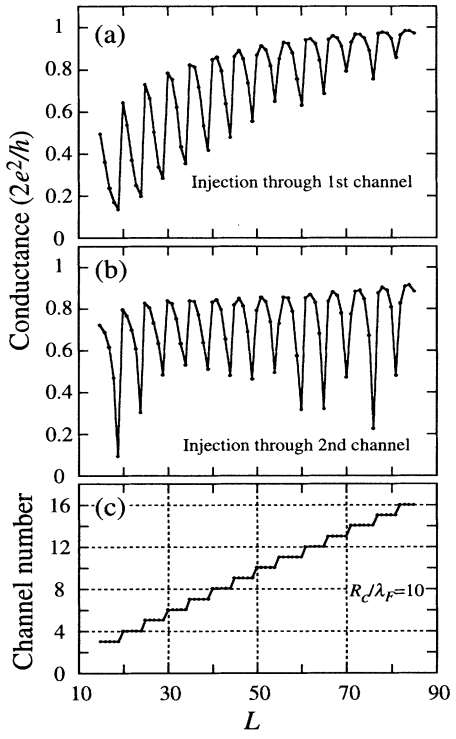

FIG. 8. Conductance from wire A with $M=20$ to wire B by changing L for an ideal abrupt structure in a magnetic field with cyclotron radius $R_c/\lambda_F=10$. (a) Injecting electron wave through the first channel and (b) through the second channel. (c) The channel number in wire B. The oscillations remain in the magnetic field, which is different from our experimental results [see Fig. 2(a)].

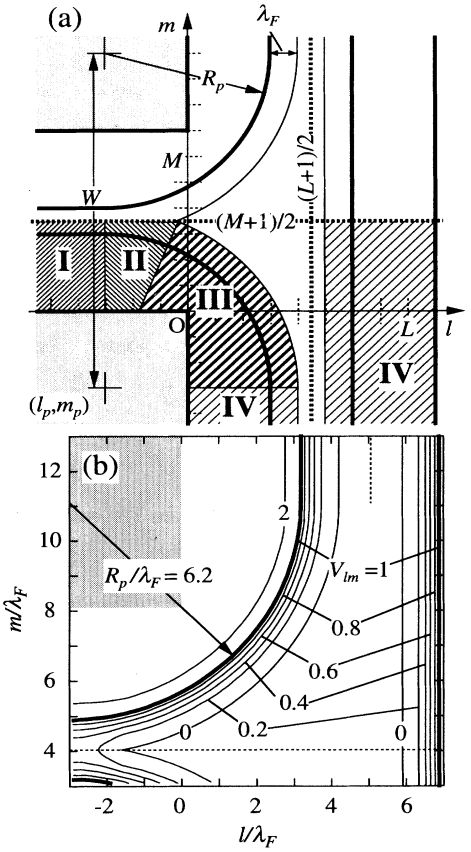

FIG. 9. (a) Schematic picture of Eqs. (4.1)–(4.4). (b) Top view of a realistic structure potential with $W=141$, $R_p=62$, $L=100$, and $M=80$. The potential energy is taken as a unit of Fermi energy E_F. Note that we did not draw higher potential lines than $V=2$, since these lines would make the figure complex.

wire A (for a point contact) and wire B (along a reflector) have a lateral potential profile composed of a parabola. We also assume that the connection between wire A and wire B has a rounded corner. As shown in Fig. 9(a), we divide the T-shaped structure into several regions, and the potential configuration has symmetry along $m=(M+1)/2$. A detailed potential profile to the four regions is given by the following expressions, for which potential energy is normalized by Fermi energy:

$$V_{lm}=\lambda_F^{-2}(m-R_p)(m+R_p-M-1)+1 , \tag{4.1}$$

when l,m are in region I in Fig. 9(a),

$$V_{lm}=1-\lambda_F^{-2}\left[\frac{W-(2m-M-1)}{W+(2m-M-1)}r_p-R_p\right](r_p-R_p) , \tag{4.2}$$

when l,m are in region II,

$$V_{lm}=\lambda_F^{-2}(r_p-R_p-\lambda_F)^2 , \tag{4.3}$$

when l,m are in region III, and

$$V_{lm}=\lambda_F^{-2}\left[\left[\frac{L+1}{2}-l_p\right]-\left|\frac{L+1}{2}-l\right|-R_p-\lambda_F\right]^2 , \tag{4.4}$$

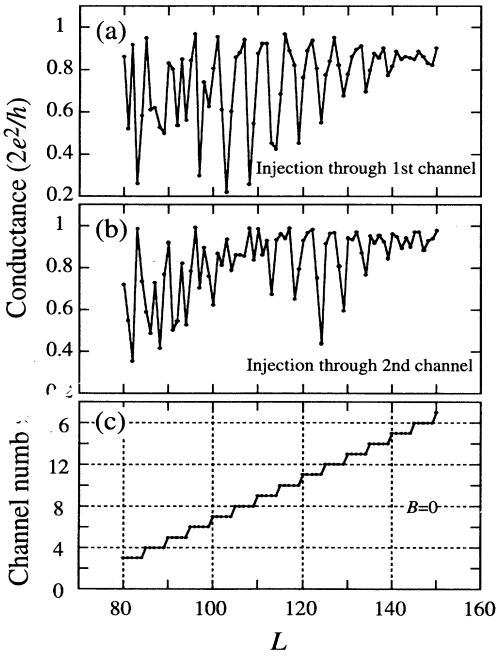

FIG. 10. Conductance from wire A to wire B by changing L. We set the Fermi wavelength $\lambda_F=10$ and assumed a realistic structure with $W=141$, $R_p=62$, and $M=80$ [see Fig. 9(b)]. (a) Injecting electron wave through the first channel and (b) through the second channel. (c) The channel number in wire B. The conductance clearly shows oscillations for a period of forming channels below the Fermi level in wire B, when the parameter $L=100-140$ (115–140) for case (a) [case (b)].

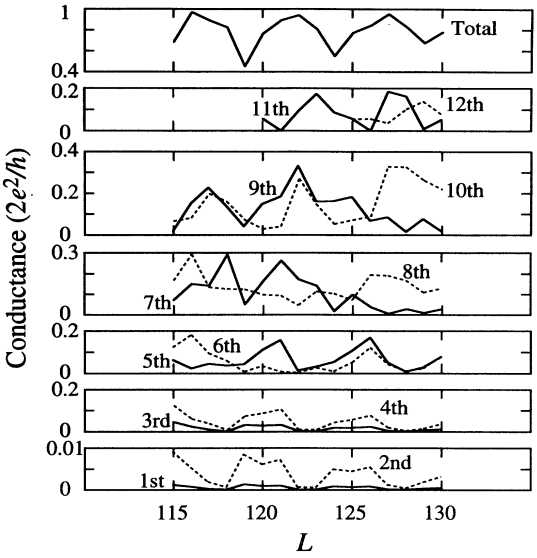

FIG. 11. Conductance contributing to each channel in wire B for a realistic structure. The periodic oscillation for a realistic structure is not only defined by matching the injected wave function against a channel just below the Fermi level.

when l,m are in region IV, where $r_p=\sqrt{(l-l_p)^2+(m-m_p)^2}$, and $l_p=m_p=-(W-M-1)/2$. In other regions, $V_{lm}=0$. The potential of a point contact has two main parameters, R_p and W. In fig. 9(a), R_p is the radius of the rounded corner, and R_p,W relate to both the metal gate structure and the width of the depletion region in the 2D electron gas. In this paper, we assume $W=141$, $R_p=62$, with $\lambda_F=10$. These values are suitable for a device with about a 0.2-μm gate length, 0.4-μm gate opening, 40-nm Fermi wavelength, and two channels in the injector below the Fermi level.[18] These dimensions are reasonable for most mesoscopic experiments. Figure 9(b) shows a top view of a point-contact potential with the above parameters. the potential profile along the m axis for the injector is completely parabolic. In the following, we use a specific value, $R_p/\lambda_F=6.2$, as a typical case of a second conductance plateau for the injector.[18]

Figure 10(a) shows the conductance as a function of L. It is more complex than Fig. 5. When the opening around a connection of quantum wires is small ($L=80-100$), the conductance oscillation is random. This might be similar to random transport of the so-called "chaotic cavity."[12,13,27] When $L>100$, the oscillations are clearly periodic. We then investigate the conductance contributing to each channel in wire B when $L=115-130$. As shown in Fig. 11, a channel just below the Fermi level contributes to the total conductance. The conductance also distributes other channels under Fermi energy more widely than in the case of Fig. 6. In Fig. 12, we show the position probability for the realistic structure. These figures show the differences between $L=116$ (matching case) in Fig. 12(a) and $L=119$ (not matching

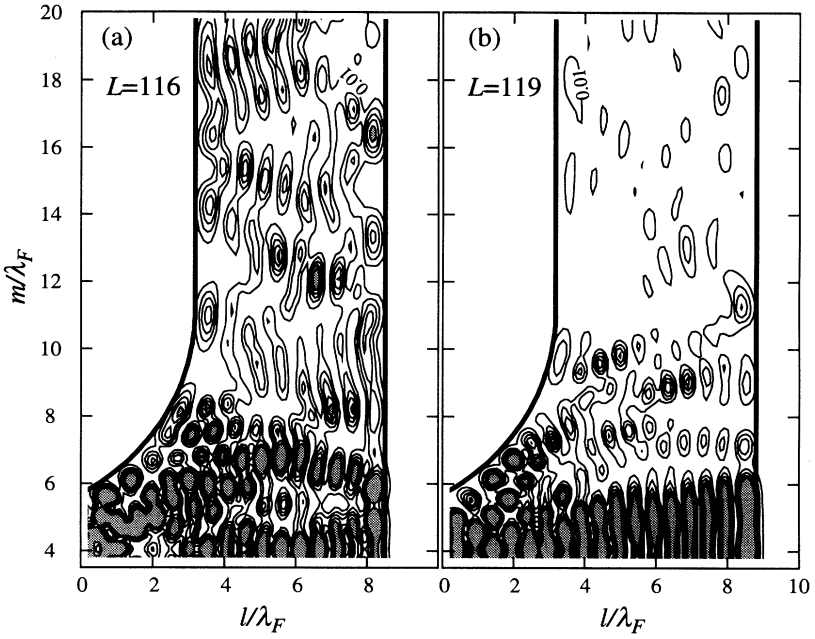

FIG. 12. Position probability density for the ideal abrupt structure. (a) $L=116$; matching case. (b) $L=119$; not matching case. Distributions of the densities have complex patterns due to multiscattering, but we clearly distinguish between cases (a) and (b). The shaded regions indicate an electron density greater than 0.05, since the contours would make the figure complex.

case) in Fig. 12(b). They also show the complex scattering phenomena. The realistic geometry leads to difficulties in the physical interpretation of the oscillations. Note that the complex scattering cannot suppress the periodic oscillation.

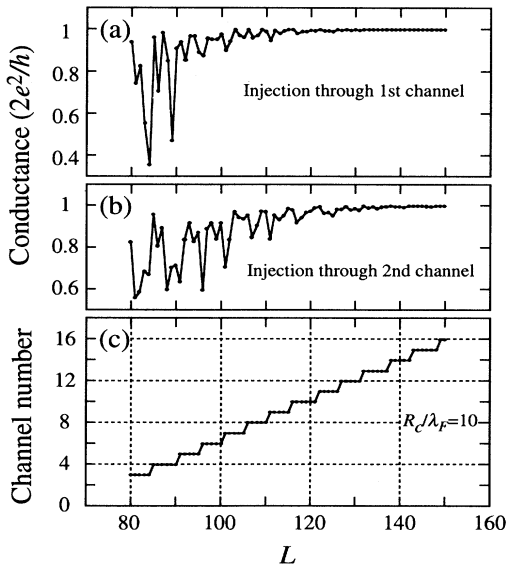

FIG. 13. Conductance from wire A to wire B by changing L for a realistic structure in a magnetic field with cyclotron radius $R_c/\lambda_F=10$. (a) Injecting electron wave through the first channel and (b) through the second channel. (c) The channel number in wire B. The oscillations are completely suppressed by the magnetic field for $L>110$. This can explain our experimental results [see Fig. 2(a)]. However, random oscillations remain for $L<110$.

Contrary to the properties in no magnetic field, the realistic structure can show a simple picture for the magnetic suppression. Figure 13 shows the conductance under a magnetic field with $R_c/\lambda_F=10$. The magnetic field eliminates the conductance oscillation when $L=115-130$. This result is quite different from that of the abrupt structure, but it agrees with our experimental results. The complete suppression is caused by the rounded corner at the connection between two wires. In order to clearly show the effects of the rounded corner, we show the position probability density in Fig. 14. Figure 14(a) shows reflections at the reflector still dominate electron-wave propagation in the ideal abrupt structure with $R_c/\lambda_F=10$. Reflections of the realistic structure in Fig. 14(b) reduce in comparison with the abrupt structure, because the magnetic field guides the electron wave along the rounded corner of the realistic structure. This guiding effect becomes clear in higher fields, and causes the suppression of classical skipping orbits. The difference between the abrupt and realistic cases is also important to analyze other experiments.[3,4,10,11]

B. Suppression of classical skipping orbit and formation of quantum edge state

Under relatively higher magnetic fields, the ballistic transport has several interesting properties. The classical skipping orbit with clear circular segments and focusing,[3] and the transport by the quantum edge states,[23] which mean channels in a quantum wire under magnetic fields here are both well-known phenomena. The magnetic focusing experiment showed the existence of a classical skipping orbit, and interesting results of numerical calculations.[8,9] There have been no numerical studies of the transition form a classical skipping orbit to quantum edge

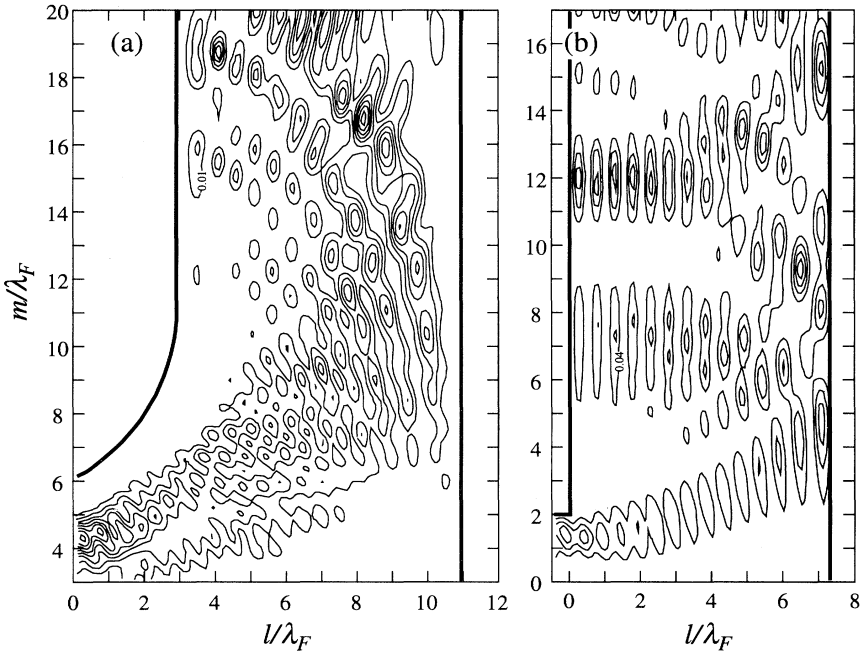

FIG. 14. Position probability density for applying magnetic field with $R_c/\lambda_F=10$. (a) $L=140$; the actual structure. (b) $L=73$; the ideal abrupt structure. These cases have seven channels under Fermi level for wire B.

state within changing magnetic fields. Our results clearly show that the transition in the realistic case is different from the abrupt case.

Figure 15 shows abrupt structure conductance for various channels while subjected to magnetic fields. Due to deflection by magnetic fields, the rising current in wire B is larger than the sinking current, even in the weak-field case with $R_c/\lambda_F=20$. The contribution of the channel just under the Fermi level remains large under a weak magnetic field with $R_c/\lambda_F=10,20$. The conductance (see Fig. 8) maintains oscillations, because the wire's width is smaller than the cyclotron radius. Under stronger fields,

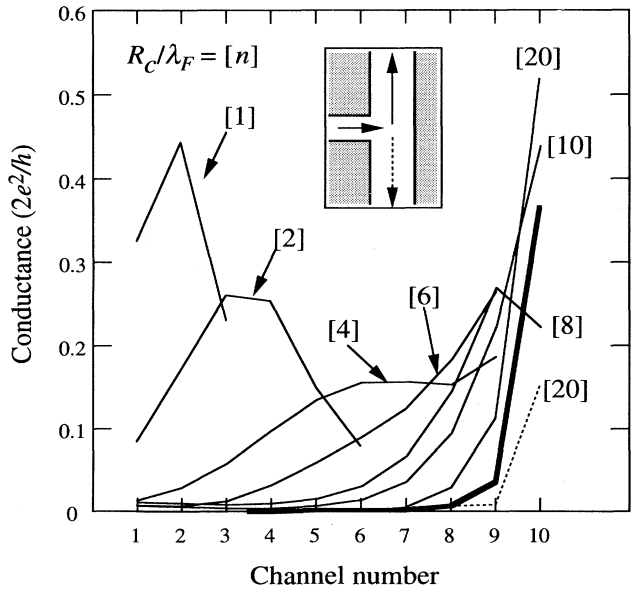

FIG. 15. Distributions of conductance at each channel in a magnetic field for an ideal abrupt structure. The broken line refers to the sinking current (see inset), and a bold line is the no magnetic field case. For a higher field $R_c/\lambda_F=1,2$, the distributions have peak structures, which indicates the formation of a classical skipping orbit.

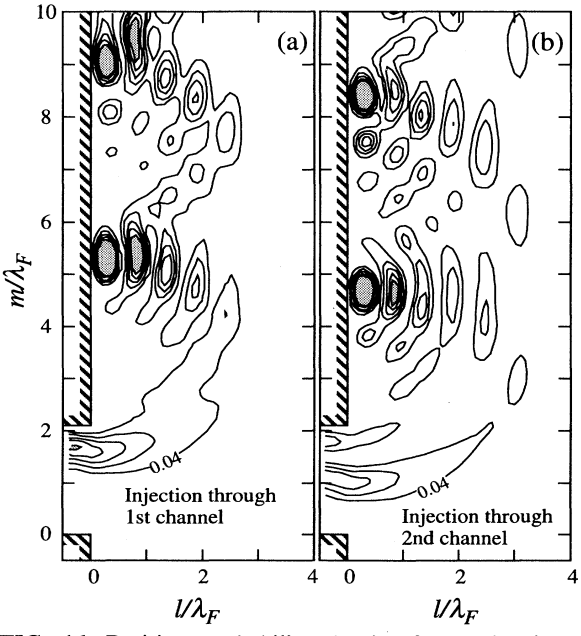

FIG. 16. Position probability density for an ideal abrupt structure in a magnetic field with $R_c/\lambda_F=2$. (a) Injecting electron wave through the first channel when $L=50, M=20$ and (b) through the second channel. These densities reveal skipping orbits with half circles and periodic magnetic focusing. The shaded regions indicate an electron density greater than 0.2, since the contours would make the figure complex.

$R_c/\lambda_F=1,2$, the distributions of the conductance contributions clearly have peak structure. This implies the formation of a classical skipping orbit. It is represented by the plane waves of several channels, in terms of the wave mechanics. In order to support this explanation, we show the position probability density in Fig. 16. The numerical results for $R_c/\lambda_F=2$ show obvious half circles, concerned with the cyclotron radius and the periodic magnetic focusing. In the case of the abrupt structure, the classical skipping orbit could be formed when an infinite wire's width is larger than the cyclotron radius. The conductance oscillation does not occur under this condition. Orbit skipping has been well investigated for an abrupt structure.[8,9] However, the propagation of electron waves through magnetic fields in a realistic structure with a rounded corner is different from the propagation in an abrupt structure.

Figure 17 shows the conductance contribution at each channel in magnetic fields for the realistic structure. In spite of deflection by magnetic fields, the rising current in the infinite wire is smaller than the sinking current when $R_c/\lambda_F=20$. This is that multiscattering for both rounded corners and reflector makes *rebounding* of electrons.[11] Under stronger fields, $R_c/\lambda_F=2,4$, the distributions of the conductance contributions have a maximum at the first (second) channels in wire B, when electron waves are injected through the first (second) channel in wire A.

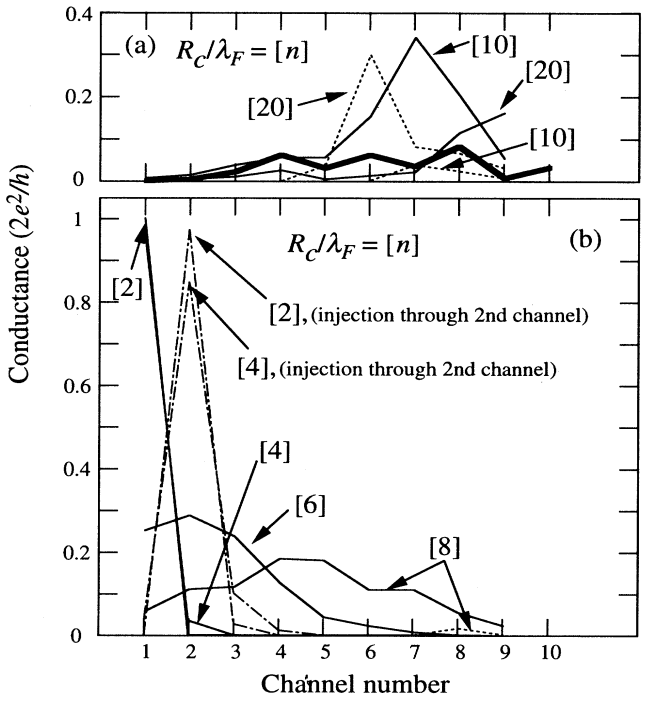

FIG. 17. Distributions of conductance at each channel in a magnetic field for a realistic structure. Broken lines refer to the sinking current (see the inset in Fig. 15), and the bold line is the no magnetic field case. For a higher field, $R_c/\lambda_F=1,2,4$, the distributions show channel selectivity, which indicates the formation of a quantum edge state.

This channel selectivity means the formation of an edge state. The position probability density in Fig. 18 clearly shows a transition from a classical skipping orbit to a quantum edge state with changing magnetic fields. For $R_c/\lambda_F=4$ in Figs. 18(a) and 18(b), the magnetic field almost guides the injected electron wave along the wall. The propagation, however, leaves both an incomplete skipping orbit and obvious magnetic focusing, especially for injection through the second channel in Fig. 18(b). For $R_c/\lambda_F=2$ in Figs. 18(c) and 18(d), the position probability densities show formation of magnetic edge states with smaller undulations. The magnetic field with $R_c/\lambda_F=2$ achieves a strong channel selectivity for the rounded corner configuration. The propagation results of the realistic structures are therefore quite different from the abrupt structure.

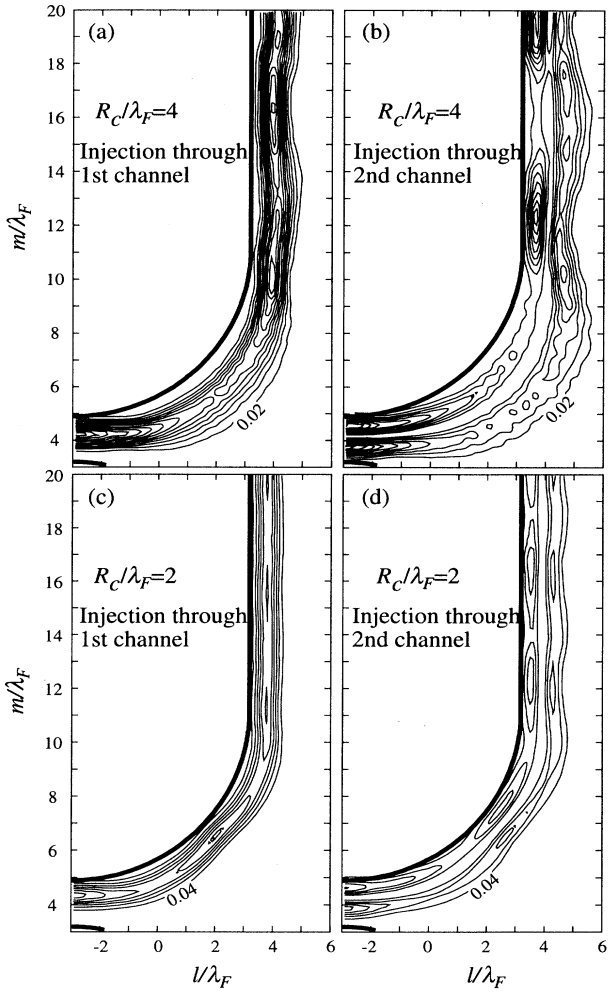

FIG. 18. Position probability density for the ideal abrupt structure in a magnetic field at $L=100$. (a) Injecting electron wave through the first channel when $R_c/\lambda_F=4$; (b) through the second channel when $R_c/\lambda_F=4$; (c) through the first channel when $R_c/\lambda_F=2$; and (d) through the second channel when $R_c/\lambda_F=2$. These numerical results show the transition from a classical skipping orbit to a quantum edge state with changing magnetic fields.

V. SUMMARY

We have described calculations based on a 2D lattice model for electron-wave propagation. Our method is a generalized technique based on the recursive Green's-function method and allows the determination of both transmission/reflection coefficients and the wave functions at an arbitrary position. It provides stable numerical results for both hard and soft confinement potentials and for both sharp and rounded geometries.

We used this method to examine ballistic electron transport in a magnetic field. The structures examined were a quantum point contact and a reflecting boundary with both realistic soft confinement potentials and rounded corners. We compared these results to those calculated for the simple case of a hard confinement potential and sharp corners.

With no magnetic field and large L, the conductance for the realistic model is clearly periodic. For small L the transport exhibited random fluctuations similar to the chaotic cavity. This is related to the strong lateral confinement between the point contact and the reflector in this regime. This effect has not been observed experimentally, probably as a result of a smearing of the complex multiscattering by inelastic scattering.

The results showed in detail the transition from a classical skipping orbit with magnetic focusing, to a quantum edge state with magnetic guiding. The trajectory of the electron wave may be determined by the competition between the magnetic effect and the collimation effect of a point contact. It is difficult to predict the trajectory in detail without a numerical calculation. Our results for soft confinement and rounded corners show both magnetic focusing and clear channel selectivity for R_c/λ_F near 4. In the case of hard confinement and sharp corners, we only found ideal skipping orbits with half circles. Therefore, there is a clear contrast between the results for rounded and sharp corners. This effect for the rounded corners shows that the experiment (especially near 1 T) for magnetic focusing and edge state requires detailed analysis.

The major results of our study relate to the magnetic-field dependence of the conductance oscillations. For the soft confinement and rounded corner model, the oscillations were found to be strongly suppressed at small magnetic fields, consistent with experimental observations. Although both the simple and realistic models show a similar oscillatory behavior with no magnetic field, the simple model cannot simulate experimental magnetic properties. Consequently, rounded boundaries are essential for the interpretation of the magnetic field dependence observed in this structure.

ACKNOWLEDGMENT

The authors thank Professor T. Ando of the University of Tokyo for his support in the University Industry Joint Research "Nano electronics."

APPENDIX

The following shows that iteration based on Eqs. (2.28)–(2.32) is also applicable to the recursive Green's-function method. By using the expressions in Ref. 21, we change $\mathbf{H}_j$ to $\tilde{\mathbf{H}}_j$, and the matrix in Eq. (2.13) is applied to a wider region as

$$\mathbf{T}_j=\begin{bmatrix} 0 & 1 \\ -\mathbf{H}_{j,j+1}^{-1}\mathbf{H}_{j,j-1} & \mathbf{H}_{j,j+1}^{-1}(E_F-\tilde{\mathbf{H}}_j) \end{bmatrix} \quad \text{for } 0\le j\le N+1 .$$

Furthermore, when an initial condition is given as

$$\mathbf{C}_1^{(0)}=(\mathbf{F}^{-1}(+)-\mathbf{F}^{-1}(-))\mathbf{U}(+) \text{ and } \mathbf{C}_2^{(0)}=\mathbf{0} ,$$

the matrices $\mathbf{C}_1^{(j+1)}$, $\mathbf{C}_2^{(j+1)}$ obtained by iteration relate to the recursive Green's function

$$\mathbf{C}_1^{(j+1)}=(j|\mathbf{G}^{(j)}|0)\mathbf{H}_{0,-1}(\mathbf{F}^{-1}(+)-\mathbf{F}^{-1}(-))\mathbf{U}(+)$$

and

$$\mathbf{C}_2^{(j+1)}=(j|\mathbf{G}^{(j)}|j)\mathbf{H}_{j,j+1} .$$

Here, Green's function $\mathbf{G}$ is defined by the following well-known relations:[21]

$$(0|\mathbf{G}^{(0)}|0)=(E_F-\tilde{\mathbf{H}}_0)^{-1} ,$$

$$(j|\mathbf{G}^{(j)}|j)=[E_F-\tilde{\mathbf{H}}_j-\mathbf{H}_{j,j-1} \times(j-1|\mathbf{G}^{(j-1)}|j-1)\mathbf{H}_{j-1,j}]^{-1} ,$$

and

$$(j|\mathbf{G}^{(j)}|0)=(j|\mathbf{G}^{(j)}|j)\mathbf{H}_{j,j-1}(j-1|\mathbf{G}^{(j-1)}|0) .$$

Then, this iteration method is a generalized calculation technique including the recursive Green's-function method and the method in Ref. 18.

*Fax: +81-462-50-8844. Electronic address: usukitty@flab.fujitsu.co.jp

[1]B. J. van Wees, H. van Houten, C. W. J. Beenakker, J. G. Williamson, L. P. Kouwenhoven, D. van der Marel, and C. T. Foxon, Phys. Rev. Lett. **60**, 848 (1988).

[2]D. A. Wharam, T. J. Thornton, R. Newbury, M. Pepper, H. Ahmed, J. E. F. Frost, D. G. Hasko, D. C. Peacock, D. A. Ritchie, and G. A. C. Jones, J. Phys. C **21**, L209 (1988).

[3]H. van Houten, C. W. J. Beenakker, J. G. Williamson, M. E. I. Broekaart, P. H. M. van Loosdrecht, B. J. van Wees, J. E. Mooij, C. T. Foxon, and J. J. Harris, Phys. Rev. B **39**, 8556 (1989).

[4]M. L. Roukes, A. Scherer, S. J. Allen, Jr., H. G. Craighead, R. M. Ruthen, E. D. Beebe, and J. P. Harbison, Phys. Rev. Lett. **59**, 3011 (1987).

[5]C. J. B. Ford, T. J. Thornton, R. Newbury, M. Pepper, H. Ahmed, D. C. Peacock, D. A. Ritchie, J. E. F. Frost, and G. A. C. Jones, Phys. Rev. B **38**, 8518 (1988).

[6]A. Kawabata, J. Phys. Soc. Jpn. **58**, 372 (1989).
[7]M. Büttiker, Phys. Rev. B **41**, 7906 (1990).
[8]A. Nakamura, Y. Maki, and A. Okiji, J. Phys. Soc. Jpn. **60**, 749 (1991); A. Okiji, H. Negishi, and A. Nakamura, *ibid.* **61**, 1145 (1992).
[9]T. Ueta, J. Phys. Soc. Jpn. **61**, 4314 (1992).
[10]C. W. J. Beenakker and H. van Houten, Phys. Rev. Lett. **63**, 1857 (1989).
[11]M. L. Roukes, A. Scherer, and B. P. Van der Gaag, Phys. Rev. Lett. **64**, 1154 (1990).
[12]M. L. Roukes and O. L. Alerhand, Phys. Rev. Lett. **65**, 1651 (1990).
[13]R. A. Jalabert, H. U. Baranger, and A. D. Stone, Phys. Rev. Lett. **65**, 2442 (1990).
[14]M. Saito, T. Usuki, M. Okada, T. Futatsugi, R. A. Kiehl, and N. Yokoyama, Appl. Phys. Lett. **65**, 3087 (1994).
[15]A. Yacoby, U. Sivan, C. P. Umbach, and J. M. Hong, Phys. Rev. Lett. **66**, 1938 (1991).
[16]D. C. Miller, R. K. Lake, S. Datta, M. S. Lundstorm, M. R. Melloch, and R. Reifenberger, in *Nanostructure Physics and Fabrication* (Academic, New York, 1989), p. 165.
[17]C. C. Eugster and J. A. Alamo, Phys. Rev. Lett. **67**, 3586 (1991). For numerical analysis of this experiment, see Y. Takagaki and D. K. Ferry, Phys. Rev. B **45**, 12 152 (1992); G. Xu, L. Jiang, D. Lu, and X. Xie, *ibid.* **51**, 2287 (1995).
[18]T. Usuki, M. Takatsu, R. A. Kiehl, and N. Yokoyama, Phys. Rev. B **50**, 7615 (1994).
[19]D. J. Thouless and S. Kirkpatrick, J. Phys. C **14**, 235 (1981).
[20]P. A. Lee and D. S. Fisher, Phys. Rev. Lett. **47**, 882 (1981).
[21]T. Ando, Phys. Rev. B **44**, 8017 (1991).
[22]R. Landauer, IBM J. Res. Dev. **1**, 223 (1957); **32**, 306 (1988).
[23]M. Büttiker, IBM J. Res. Dev. **32**, 317 (1988).
[24]D. S. Fisher and P. A. Lee, Phys. Rev. B **23**, 6851 (1981).
[25]M. Saito, M. Takatsu, M. Okada, and N. Yokoyama, Phys. Rev. B **46**, 13 220 (1992).
[26]S. E. Laux, D. J. Frank, and Frank Stern, Surf. Sci. **196**, 101 (1988).
[27]H. U. Baranger and P. A. Mello, Phys. Rev. Lett. **73**, 142 (1994).

(a)

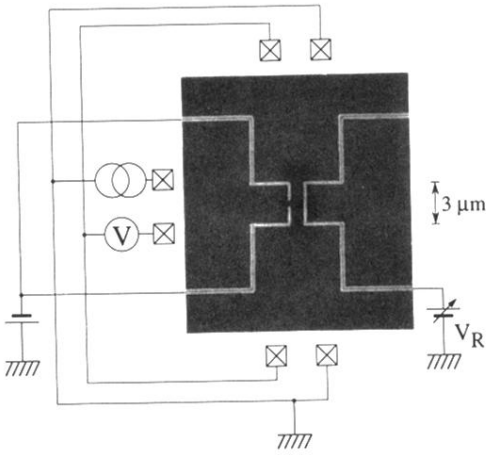

(b)

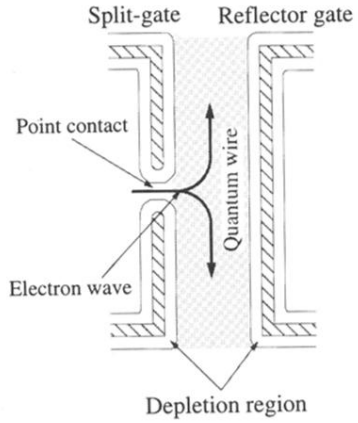

FIG. 1. (a) A scanning electron microscope micrograph of our device with control and measurement circuits for point-contact resistance. (b) Diagram of a confinement structure with a point contact and a reflector. The shaded region indicates a quantum wire with 1D channels, where the 1D channel number is controlled by changing the voltage V_R.

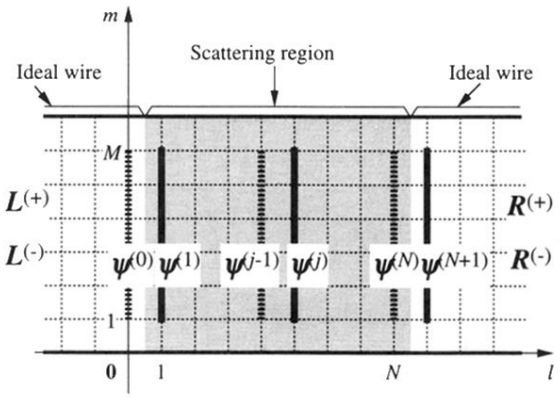

FIG. 3. Configuration of a lattice model for a quantum wire. Integer coordinates (l,m) mean lattice points, and the lattice constant is taken as a unit of length. This model consists of a scattering region and two ideal wires of width $M+1$.

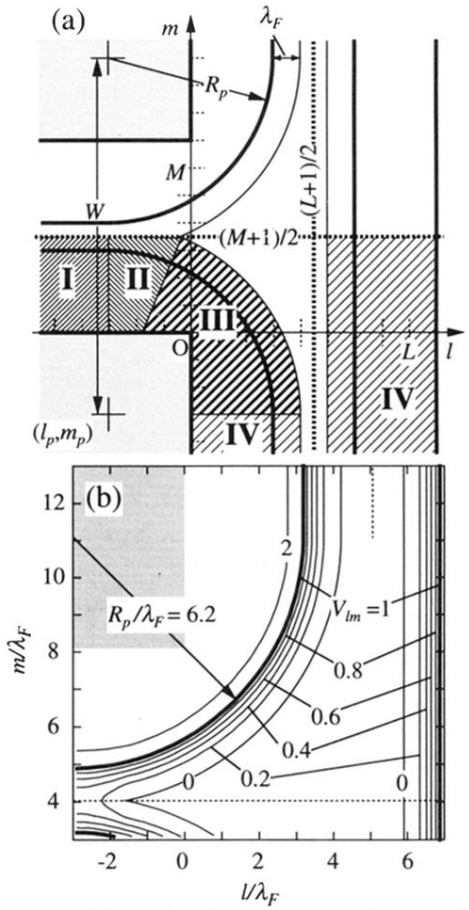

FIG. 9. (a) Schematic picture of Eqs. (4.1)–(4.4). (b) Top view of a realistic structure potential with $W=141$, $R_p=62$, $L=100$, and $M=80$. The potential energy is taken as a unit of Fermi energy E_F. Note that we did not draw higher potential lines than $V=2$, since these lines would make the figure complex.